Reduced Graphene Oxide-Modified Carbon Nanotube/Polyimide Film Supported MoS_2 Nanoparticles for Electrocatalytic Hydrogen Evolution

*Yimin Jiang, Xin Li, Shengjiao Yu, Lingpu Jia, Xiaojuan Zhao, and Chunming Wang**

Efficient evolution of hydrogen through electrocatalysis at low overpotentials holds tremendous promise for clean energy. Herein, a highly active and stable MoS_2 electrocatalyst is supported on reduced graphene oxide-modified carbon nanotube/polyimide (PI/CNT-RGO) film for hydrogen evolution reaction (HER). The PI/CNT-RGO film allows the intimate growth of MoS_2 nanoparticles on its surface. The nanosize and high dispersion of MoS_2 nanoparticles provide a vast amount of available edge sites and the coupling of RGO and MoS_2 enhances the electron transfer between the edge sites and the substrate, greatly improving the HER activity of PI/CNT-RGO-MoS_2 film. The MoS_2 with a smaller loading less than 0.04 mg cm^{-2} on the PI/CNT-RGO film exhibits excellent HER activities with a low overpotential of 0.09 V and large current densities, as well as good stability. The Tafel slope of 61 mV dec^{-1} reveals the Volmer–Heyrovsky mechanism for HER. Thus, this work paves a potential pathway for designing efficient MoS_2-based electrocatalysts for HER.

1. Introduction

Hydrogen is being vigorously pursued as a future energy carrier in the transition from hydrocarbon economy.[1] In particular, sustainable hydrogen production through water splitting has attracted growing attention.[2,3] The electrochemical hydrogen evolution reaction (HER) requires advanced electrocatalysts with a high current density at a low overpotential. Most effective HER electrocatalysts in acidic media are based on noble metals, such as Pt and Pd.[4,5] However, the large-scale application of noble metals is limited by their high cost and low abundance. Thus, developing effective HER electrocatalysts with high abundance and low cost still remains challenging.[6,7] Recently, many alternatives for Pt-based electrocatalysts have been widely investigated, such as transition-metal chalcogenides,[8–10] carbides,[11] borides,[12] and a family of molecular catalysts.[13,14] Among these alternatives, MoS_2 has received tremendous attention because of its earth-abundant composition and high activity, greatly promoting the development of MoS_2-based HER electrocatalysts.[15]

Y. M. Jiang, X. Li, S. J. Yu, L. P. Jia,
X. J. Zhao, Prof. C. M. Wang
State Key Laboratory of Applied Organic Chemistry
College of Chemistry and Chemical Engineering
Lanzhou University
Lanzhou 730000, P.R. China
E-mail: wangcm@lzu.edu.cn

DOI: 10.1002/adfm.201500194

As a typical transition-metal dichalcogenide, MoS_2 is a promising electrocatalyst for HER. Both computational and experimental results have confirmed that the HER activity of MoS_2 stemmed from the sulfur edges, whereas the basal planes were catalytically inert.[16,17] As a result, nanosized MoS_2 should be more active for HER electrocatalysis than the relatively inert bulk forms due to the presence of more exposed sulfur edges. Besides, the electrical conductivity of catalysts is crucial to the catalytic activity because a high conductivity can ensure a fast electron transfer during a catalytic process.[18,19] It is well-known that MoS_2 exhibits poor intrinsic conductivity originated from its large bandgap,[20] which significantly limits the overall HER rate. The past years have witnessed expanding endeavors in improving the conductivity of MoS_2-based electrocatalysts. Carbon materials have been widely used to improve the catalytic activity of MoS_2, relying on their unique physicochemical properties. Dai and co-workers synthesized MoS_2/RGO composite and achieved high HER catalytic activity at a low overpotential.[21] Chorkendorff and co-workers reported a highly active and stable carbon fibre/MoS_x composite for electrochemical hydrogen evolution.[22] Cheng and co-workers synthesized CoS_2/RGO-CNT composites for high efficient HER electrocatalysts.[23] Such findings suggest the significance of carbon materials in HER electrocatalysis. MoS_2/carbon composites have been successfully applied for the electrocatalytic HER, where carbon materials play the role of hosting MoS_2 as well as enhancing the conductivity of the composites.

Although the HER properties of MoS_2/carbon composites have been investigated, the electrocatalytic activity of MoS_2 supported on carbon materials in the form of a conducting polymer film has not been studied. In this work, we synthesized MoS_2 on the reduced graphene oxide-modified carbon nanotube/polyimide (PI/CNT-RGO) film by an electrochemical method. CNT can greatly improve the mechanical and electrical properties of CNT/polymer composites, leading to the good conductivity and mechanical properties of PI/CNT film.[24,25] PI/CNT film can be used over a wide temperature range of −200 to 300 °C and in the condition of strong acid or alkaline. We prepared PI/CNT film and modified the film with RGO which further improved the conductivity of PI/CNT film and affected the morphology of MoS_2. Finally, the obtained PI/CNT-RGO-MoS_2

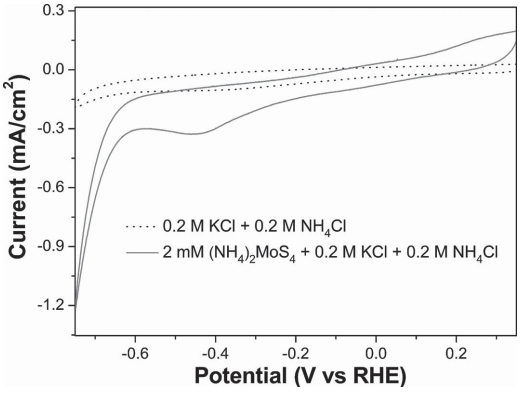

Figure 1. CVs of the PI/CNT-RGO film in 0.2 M KCl and 0.2 M NH_4Cl with 2×10^{-3} M $(NH_4)_2MoS_4$.

film by a simple electrodeposition was directly applied in HER electrocatalysis, superior to the usual MoS_2-based composites by hydrothermal or solvothermal reactions which still relied on a basal electrode to achieve HER electrocatalysis. The MoS_2 on the PI/CNT-RGO film exhibited excellent HER activity at a low overpotential and with high current densities.

2. Results and Discussion

2.1. Electrochemical Characteristics

The electrochemical behaviors of the PI/CNT-RGO film towards $(NH_4)_2MoS_4$ were investigated by cyclic voltammograms (CV). **Figure 1** shows the current responses of the PI/CNT-RGO film toward 2.0×10^{-3} M $(NH_4)_2MoS_4$ in 0.2 M KCl and 0.2 M NH_4Cl. No redox peaks were observed when CV measurements were performed in the blank solution without $(NH_4)_2MoS_4$, confirming the stability of the PI/CNT-RGO film in the potential region. When 2.0×10^{-3} M $(NH_4)_2MoS_4$ was added in the blank solution, a well-defined cathodic peak occurred at –0.45 V with a significant increase of peak current, corresponding to the reduction reaction of $(NH_4)_2MoS_4$ as follows

$$MoS_4^{2-} + 2H_2O + 2e^- \rightarrow MoS_2 + 2SH^- + 2OH^- \quad (1)$$

No stripping peaks appeared during the anodic scanning, revealing that the reduction of $(NH_4)_2MoS_4$ was irreversible, which provided an opportunity for the deposition of MoS_2.

2.2. Structure and Morphology

The morphology of MoS_2 for 15 CVs was characterized by field emission scanning electron microscopy (SEM) (**Figure 2**a), which clearly showed the nanoparticle morphology. The SEM image with lower magnification and size distribution of MoS_2 nanoparticles in Figure S1 (Supporting Information) indicated that RGO sheets were decorated with uniformly dispersed MoS_2 nanoparticles and the diameter of nanoparticles was mainly in the range of 180–200 nm. A corresponding transmission electron microscopy (TEM) image also verified the nanoparticle morphology of MoS_2 (Figure 2b). The light contrast in various areas of TEM image showed that MoS_2 nanoparticles lay flat on the RGO sheets, which was further confirmed by the TEM image of a single MoS_2 nanoparticle (Figure S2, Supporting Information). The high-resolution transmission electron microscopy (HRTEM) image of a single nanoparticle was shown in Figure 2c, in which a lattice spacing of 0.27 nm was observed, consistent with the *d* spacing of (100) planes of hexagonal MoS_2. In addition, the HRTEM image presented that the directions of individual (100) planes on the basal surface had a slight rotation from each other, generating a relatively disordered atomic arrangement which caused the cracking of basal planes and thus resulted in the formation of additional edges.[15] Two diffraction rings were evident in the selected area electron diffraction (SAED) pattern (Figure 2d), in which the diffraction ring for (100) planes exhibited much brighter, suggesting the preferential crystal growth of MoS_2 nanoparticles along the (100) planes.

To further disclose the crystal structure of MoS_2, the MoS_2 nanoparticles were characterized by X-ray diffraction (XRD) (Figure 2e). All the diffraction peaks matched the hexagonal structure of MoS_2 (JCPDS 37–1492), in which the (100) diffraction peak displayed the highest intensity, indicating the preferential growth of (100) planes, consistent with the result of SAED pattern. It was worth noting that the diffraction peak at 14° for (002) planes was not observed. As previously reported, the MoS_2 by electrodeposition was usually amorphous and lacked good crystallinity, which caused poor diffraction peaks in XRD pattern.[26] The MoS_2 electrodeposited on the PI/CNT-RGO film induced three peaks, suggesting the partly crystallized structure, which was in good agreement with the results of HRTEM and SAED. Besides, a broad diffraction peak was observed at 25.22° in the XRD pattern, corresponding to the (002) planes of RGO.[27] Raman spectroscopy revealed the typical peaks of MoS_2 and the D, G bands of RGO in the sample (Figure 2f).[28,29] Two apparent peaks at 381 and 405 cm^{-1} were attributed to the $E_{2g}{}^1$ and A_{1g} vibrational modes of MoS_2 (Figure S3, Supporting Information). In the higher wavelength region, the peaks at 1350 and 1593 cm^{-1} corresponded to the D and G bands of RGO.

X-Ray photoelectron spectroscopy (XPS) was used to confirm the chemical state and composition of MoS_2. The survey spectrum revealed that the sample contained the elements of Mo, S, C, and O and the atomic ratio of Mo/S was 1:2 (**Figure 3**a). The C 1s spectrum in Figure 3b showed a dominated C=C peak with a small peak related to oxygen-containing groups, confirming the effective reduction of GO to RGO.[30] Two peaks at 229.7 and 232.8 eV in Figure 3c were attributed to Mo $3d_{5/2}$ and $3d_{3/2}$ binding energies for a Mo(IV) oxidation state.[31,32] The weak peak at 226.8 eV was assigned to S 2s. The peaks for S 2p in Figure 3d were observed at 161.9 and 163.1 eV, corresponding to the S $2p_{3/2}$ and $2p_{1/2}$ orbits of divalent sulfide ions (S^{2-}).[33] These XPS data confirmed the formation of MoS_2 on the PI/CNT-RGO film.

PI/CNT-RGO film provided a substrate for the nucleation and subsequent growth of MoS_2 and the catalytic activity of MoS_2 depended on the thickness, thus we studied the morphology evolution of MoS_2 on the PI/CNT-RGO film. The SEM

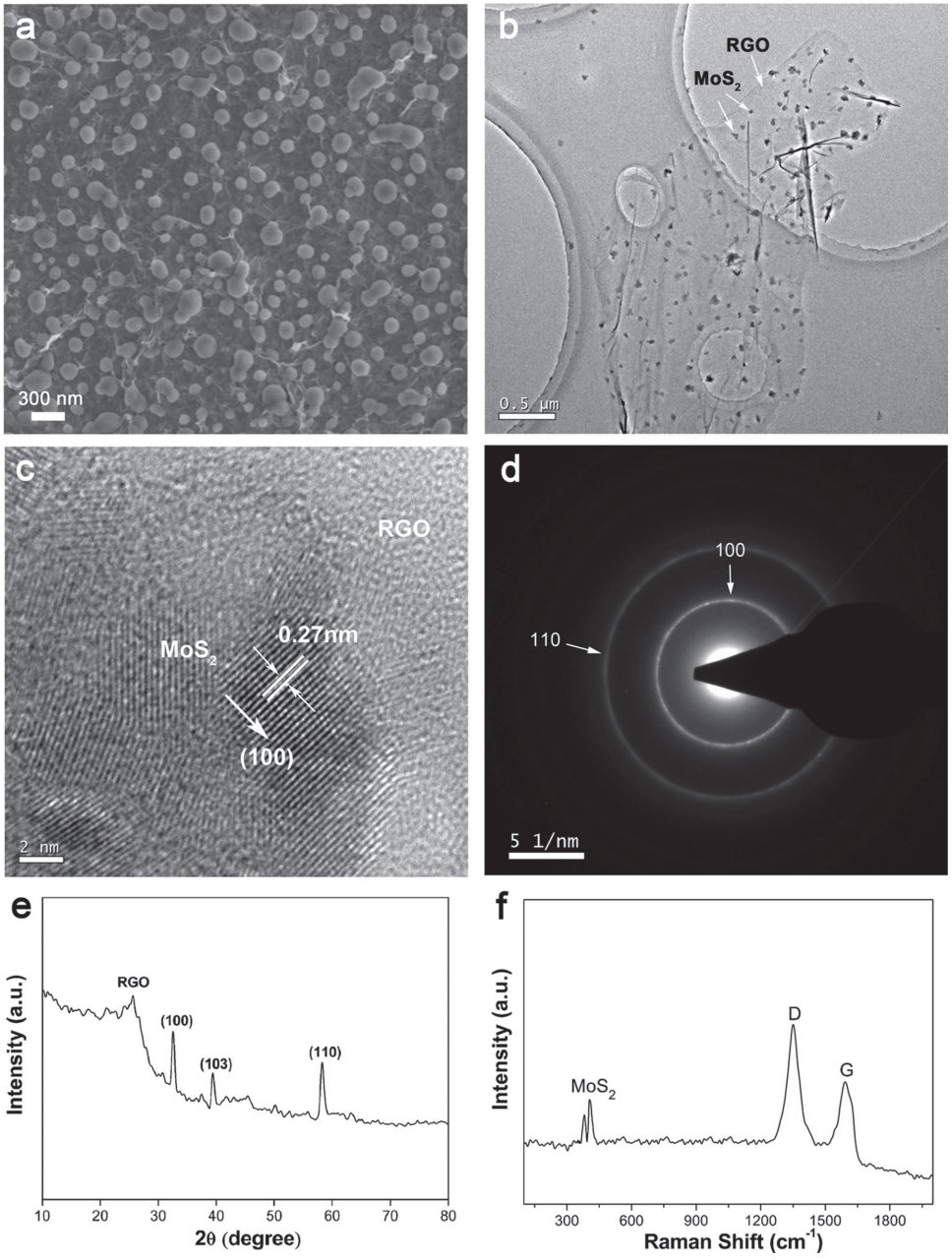

Figure 2. Characterizations for MoS_2 on the PI/CNT-RGO film: a) SEM image; b,c) TEM and HRTEM images; d) SAED pattern; e,f) XRD pattern and Raman spectrum.

images at different growth stages were shown in **Figure 4**. At the first stage for 5 CVs, a small number of MoS_2 nanoparticles were formed on the PI/CNT-RGO film with a size of 40–50 nm (Figure 4a). As the scanning increased to 10 CVs, more nanoparticles with a larger size of 80–100 nm were observed (Figure 4b). After 15 CVs, the PI/CNT-RGO film was decorated with a vast amount of free MoS_2 nanoparticles (Figure 4c), which were of 180–200 nm in diameter. From 5 to 15 CVs, an increasing number of free MoS_2 nanoparticles were formed on the PI/CNT-RGO film. As the reaction continued to 20 CVs, the MoS_2 nanoparticles spontaneously aggregated into larger nanospheres (Figure 4d), which stacked with each other. Here, a compact MoS_2 film appeared and the original nanoparticles were no longer evident. A further increase of scanning cycle to 25 CVs generated a dense MoS_2 film with a few cracks (Figure 4e), on which there were a few MoS_2 nanospheres. As the reaction continued to 30 CVs, the morphology of MoS_2 was not greatly changed except for the more seriously cracked structure (Figure 4f). Taken together, the PI/CNT-RGO film allowed the intimate growth of highly dispersed MoS_2 nanoparticles on its surfaces because of the strong interactions between PI/CNT-RGO film and MoS_2 nanoparticles,[34,35] which significantly increased the sulfur edge sites, benefiting the HER electrocatalytic activity of MoS_2.[36]

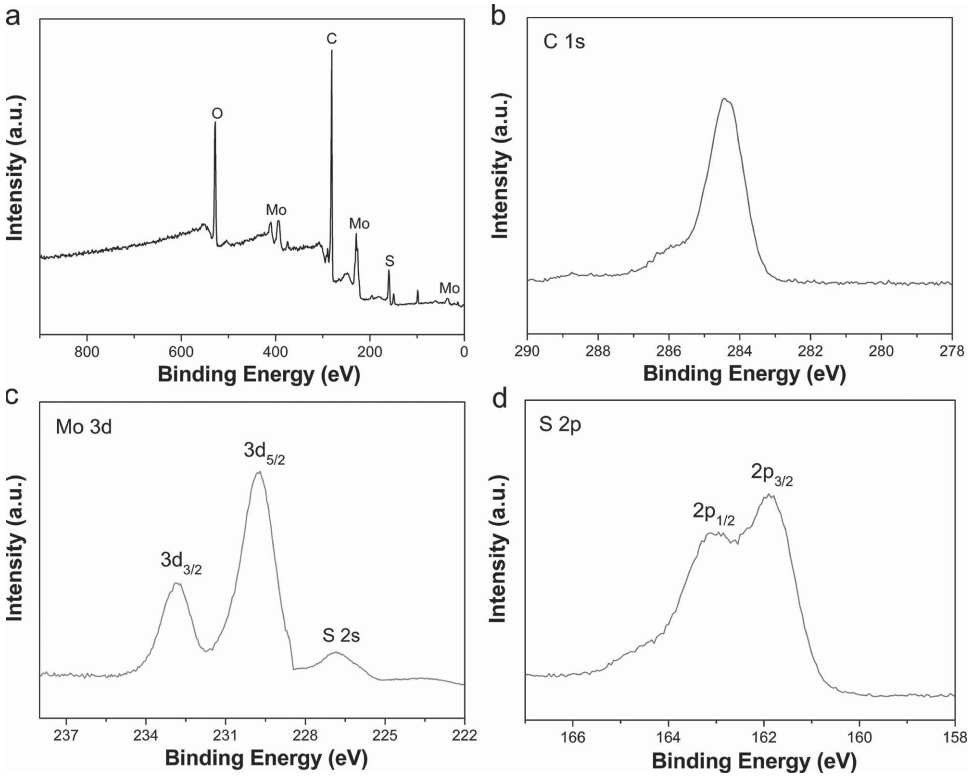

Figure 3. XPS of MoS_2 on the PI/CNT-RGO film: a) Survey spectrum; b) C 1s spectrum; c) Mo 3d spectrum; d) S 2p spectrum.

2.3. HER Electrocatalytic Activities of MoS_2

The HER electrocatalytic activities of MoS_2 obtained at different growth stages were performed in 0.5 M H_2SO_4 using a three-electrode setup. The polarization curves in **Figure 5**a revealed that the MoS_2 for 15 CVs showed a small overpotential of ≈0.09 V, beyond which cathodic current increased rapidly under more negative potentials. In contrast, the samples for 5, 10, 20, 25, and 30 CVs exhibited relatively poor HER activities in terms of the onset potential and current density. The HER electrocatalytic activity of MoS_2 is correlated with the number of exposed sulfur edge sites.[17] With the scanning from 5 to 15 CVs, an increasing number of free MoS_2 nanoparticles were formed on the PI/CNT-RGO film, which afforded more active edge sites for HER,[37] whereas the further increase of scanning cycle resulted in the decreases of active edge sites due to the aggregated and stacked morphology. Therefore, the optimum scanning cycle for MoS_2 was 15 CVs and the MoS_2 for 15 CVs showed excellent HER activity. In order to better evaluate the HER activities of MoS_2 on the PI/CNT-RGO film, we compared the HER activities of the MoS_2 and other HER electrocatalysts (**Table 1**). The MoS_2 with a smaller loading in this work achieved large current densities at low potentials, which was comparable or superior to other HER electrocatalysts.

Tafel plots of various samples were investigated to obtain further insight into the HER (Figure 5b). The linear portion of Tafel plot is fit to Tafel equation $\eta = b\log j + a$, where η is the overpotential, j is the current density, and b is the Tafel slope. The Tafel slope of MoS_2 for 15 CVs was 61 mV dec^{-1}, which was consistent with several earlier reported values for MoS_2.[8,15] The samples for 5, 10, 20, 25, and 30 CVs showed higher Tafel slopes of 95, 79, 72, 88, and 103 mV dec^{-1} respectively, which revealed that the MoS_2 for 15 CVs with a small Tafel slope was more active than the rest samples. The improved electrocatalytic activity of MoS_2 may be attributed to the optimized amount of catalytic edge sites from highly dispersed MoS_2 nanoparticles.[34] The optimal HER catalyst is the material that gives the highest current at the least overpotential and this catalyst has a low Tafel slope and a large exchange current density. A lower Tafel slope means that a catalyst requires a lower overpotential to produce a required current and a low overpotential means that there are adequate sites for reaction. The PI/CNT-RGO-MoS_2 samples afford different number of active edge sites for HER, resulting in the difference in overpotentials and Tafel slopes. A small Tafel slope can lead to a fast HER rate, which is advantageous for the practical applications of HER.

To directly investigate the effect of active edge sites provided by free MoS_2 nanoparticles, the polarization curves of MoS_2 on the PI/CNT and PI/CNT-RGO films were performed (**Figure 6**a). For comparison, the polarization curves of the PI/CNT and PI/CNT-RGO films were also recorded, showing negligible cathodic currents, which revealed that the two bare films were inactive for HER. The MoS_2 on the PI/CNT-RGO film displayed a much smaller overpotential with a faster increase of cathodic current, suggesting a better HER electrocatalytic activity than the MoS_2 on the PI/CNT film. The corresponding Tafel plots in Figure 6b presented a larger Tafel slope of 109 mV dec^{-1} for the MoS_2 on the PI/CNT film. Compared with the MoS_2 on the PI/CNT film, the MoS_2 samples on the PI/CNT-RGO

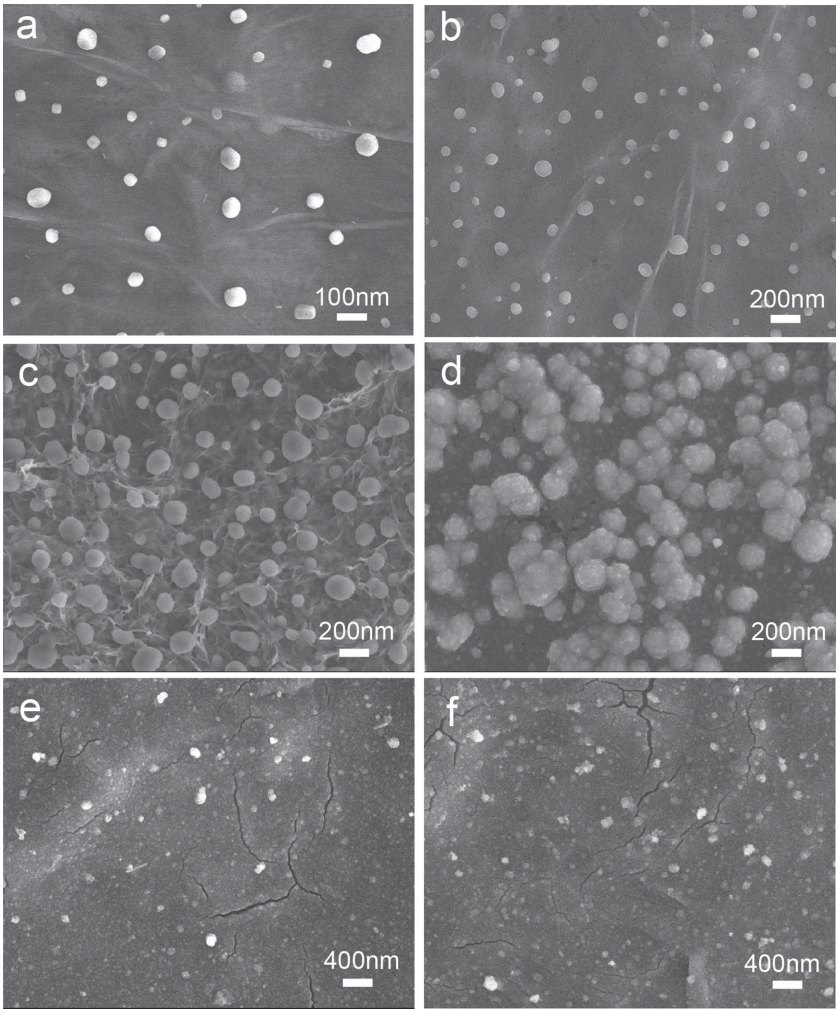

Figure 4. SEM images of MoS_2 at different growth stages (CVs): a) 5, b) 10, c) 15, d) 20, e) 25, f) 30.

film exhibited smaller Tafel slopes and larger current densities (Figures 5 and 6), which demonstrated that RGO skeleton played a pivotal role in improving the HER performance of MoS_2. The SEM image of MoS_2 on the PI/CNT film in Figure 6c showed irregular morphology. The MoS_2 nanoparticles on the surface of PI/CNT film acted as the nucleation sites for further growth of nanoparticles, leading to the formation of island-like structure which greatly decreased the edge sites for HER.

Figure 7 shows the schematic illustration of the HER electrocatalytic mechanism on the PI/CNT-RGO-MoS_2 film. RGO reduced the aggregation of MoS_2 nanoparticles and controlled the growth of dispersed nanoparticles, which increased the exposure of active edge sites. The enhanced electrocatalytic activity of MoS_2 was also attributed to the strong chemical and electronic coupling between RGO and MoS_2, providing rapid electron transport between the active edge sites and PI/CNT-RGO film. To verify our hypothesis, the impedance measurements were performed at an overpotential of 0.12 V in 0.5 M H_2SO_4. The PI/CNT-RGO-MoS_2 film exhibited lower impedance than the PI/CNT-MoS_2 film and afforded a superior HER kinetics (Figure S4, Supporting Information). Collectively, the nanoscale and high dispersion of MoS_2 nanoparticles provided an abundance of available edge sites and the coupling between RGO and MoS_2 enhanced the electron transfer between the edge sites and the substrate, which improved the HER activity of PI/CNT-RGO-MoS_2 film.

2.4. Mechanism of HER at the MoS_2 on the PI/CNT-RGO Film

Tafel slope has often been used to identify the mechanism and rate-limiting step of HER. According to the classic theory on the mechanism of hydrogen evolution, three principle steps for converting H^+ to H_2 have been proposed for the HER in acidic media.[45,46] First is a primary discharge step (Volmer reaction)

$$H_3O^+ + e^- \rightarrow H_{ads} + H_2O \quad (2)$$

which is followed by either an electrochemical desorption step (Heyrovsky reaction),

$$H_{ads} + H_3O^+ + e^- \rightarrow H_2 + H_2O \quad (3)$$

or a recombination step (Tafel reaction)

$$H_{ads} + H_{ads} \rightarrow H_2 \quad (4)$$

Tafel slope is an inherent property of a catalyst determined by the rate-limiting step of HER. Under certain conditions, when the Volmer reaction is the rate-limiting step, a slope of 120 mV dec^{-1} should be obtained, whereas if Heyrovsky or Tafel reaction acts as the rate-limiting step, the Tafel slope can reach 40 or 30 mV dec^{-1}.[45,46] For a complete HER, the combinations of Volmer–Heyrovsky or Volmer–Tafel mechanism should be involved to produce molecular hydrogen. The Tafel slope of 61 mV dec^{-1} for MoS_2 nanoparticles indicated that the rate-limiting step was the electrochemical desorption and the Volmer–Heyrovsky mechanism (Equations (2) and (3)) was operative in the HER. Although the HER mechanism for MoS_2 still remains inconclusive due to the complexity of HER, the Tafel slope in this work is close to the values in the literatures,[18,22] suggesting a similar surface chemistry of MoS_2 on the PI/CNT-RGO film to that of other HER electrocatalysts.

By applying the extrapolation method to Tafel plots, exchange current densities (j_0) of various samples were obtained (Figure S5 and Table S1, Supporting Information). As shown in **Table 2**, the MoS_2 for 15 CVs exhibited the smallest Tafel slope of 61 mV dec^{-1} and the largest j_0 of 11.48 μA cm^{-2}, indicating the best HER electrocatalytic activity among all the tested samples. In principle, a lower Tafel slope means that a catalyst requires a lower applied overpotential to generate a required current and j_0 is a measure of the electron transfer rate of a catalyst.

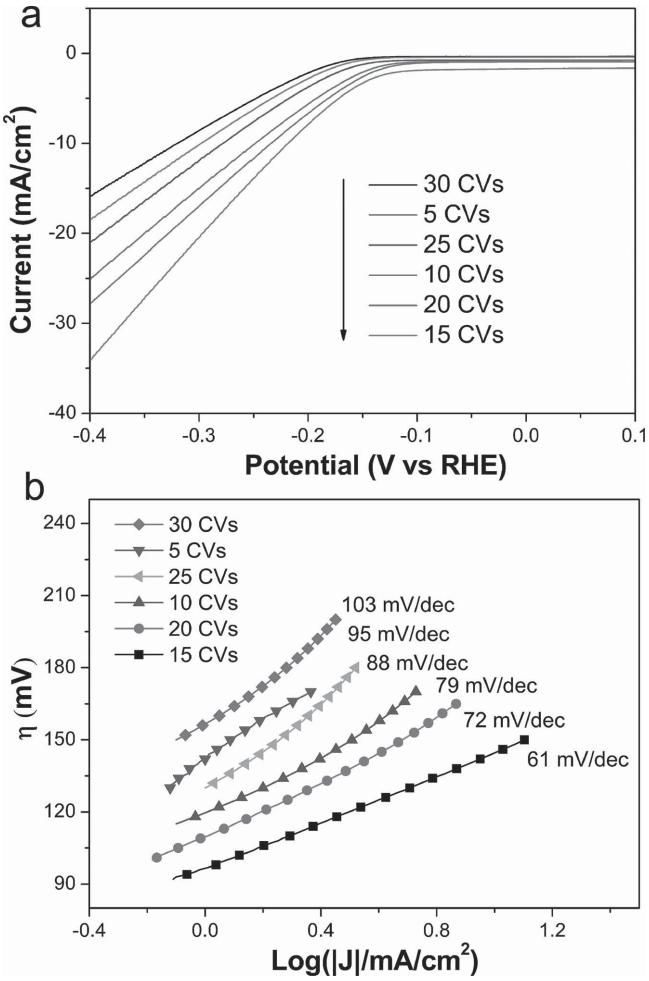

Figure 5. a) Polarization curves of MoS_2 with different scanning cycles. b) Corresponding Tafel plots of the samples in (a).

2.5. Stability

Besides the HER activity, stability was another significant criterion to evaluate a catalyst. In order to investigate the stability of the PI/CNT-RGO-MoS_2 film in acidic environment, continuous HER at a constant overpotential and a long-term cycling test were performed. A continuous HER process occurred to generate molecular hydrogen at an overpotential of 250 mV (**Figure 8**a). The current density exhibited only slight degradation after a long period of 6000 s, which may be attributed to the consumption of H^+ or the accumulation of H_2 bubbles on the film surface that hindered the HER. The polarization curves before and after 500 cycles in 0.5 M H_2SO_4 were shown in Figure 8b. After a long-term cycling, the film afforded similar polarization curves as before with negligible decrease of current density, which indicated the good stability of PI/CNT-RGO-MoS_2 film.

Table 1. Comparison of HER activities for the MoS_2 and other HER electrocatalysts. (*J* is the current density.)

Materials	*J* (−0.1 V) [mA cm^{-2}]	*J* (−0.2 V) [mA cm^{-2}]	Loading weight [mg cm^{-2}]	Ref.
MoS_2	1	40	0.136	[38]
MoS_2	2.5	14	0.285	[15]
MoS_2/RGO	1	25	0.285	[22]
MoS_2/RGO	1.5	8	0.116	[39]
$MoSe_2$	1	11	0.28	[40]
MoS_3	0.5	10	–	[41]
MoP	1	5	0.071	[42]
Mo_2C	0.2	10	0.357	[43]
MoS_2/graphene	0.5	14	0.22	[44]
MoS_2	3	13	<0.04	This work

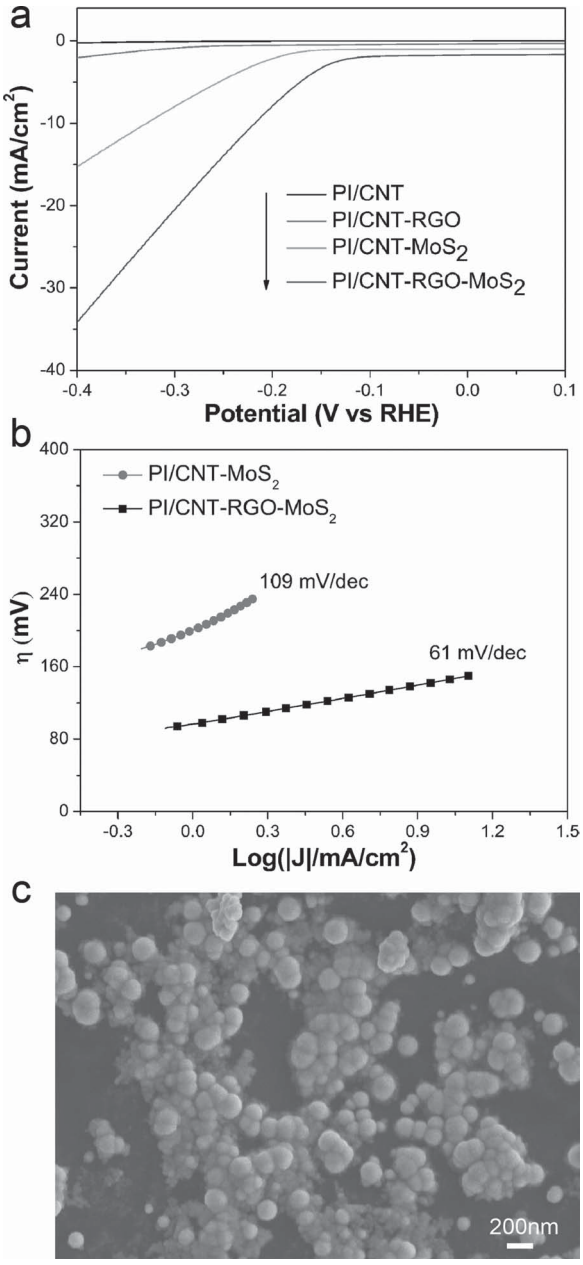

Figure 6. a) Polarization curves of MoS_2 on the PI/CNT and PI/CNT-RGO films. b) Corresponding Tafel plots of samples in (a). c) SEM image of MoS_2 on the PI/CNT film.

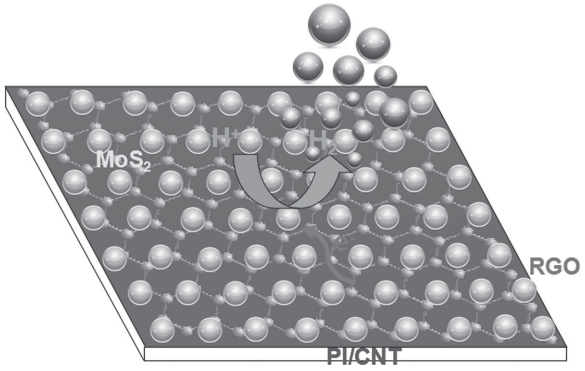

Figure 7. Schematic illustration of the electrocatalytic mechanism on the PI/CNT-RGO-MoS_2 film.

The SEM image of MoS_2 after 500 cycles showed that the nanoparticle morphology of MoS_2 exhibited no obvious changes after a long-term cycling test (Figure S6, Supporting Information), which confirmed the good stability of the MoS_2 nanoparticles under a long-term cycling process.

3. Conclusions

In conclusion, we synthesized MoS_2 nanoparticles on the PI/CNT-RGO film by an electrochemical method and achieved high HER electrocatalytic activity at a low overpotential. Free MoS_2 nanoparticles uniformly dispersed on the PI/CNT-RGO film, leading to the nanoscale and high dispersion of MoS_2 nanoparticles which provided an abundance of available edge sites for HER. With the highly exposed edge sites and the coupling between RGO and MoS_2, the MoS_2 with a smaller loading less than 0.04 mg cm^{-2} on the PI/CNT-RGO film achieved excellent HER electrocatalytic activity with a low overpotential of 0.09 V and large current densities. A Tafel slope of 61 mV dec^{-1} revealed the rate-limiting step of the electrochemical desorption in HER. The synergetic coupling between MoS_2 and RGO on the PI/CNT film efficiently improved the HER activity of MoS_2, opening up a brand new way to advanced electrocatalysts for energy conversion.

4. Experimental Section

Preparation of PI/CNT-RGO-MoS_2 Film: PI/CNT film was prepared as previously described.[47,48] GO was synthesized by a modified Hummers method.[49] 10 μL GO solution (1 mg mL^{-1}) was loaded onto the PI/CNT film, which was dried at room temperature. To obtain the PI/CNT-RGO film, the electrochemical reduction of GO was performed in 0.1 M Na_2SO_4 with a potential scanning from 0.6 to −1.2 V at 10 mV s^{-1} for 10 cycles. The deposition of MoS_2 was carried out on CHI 660 electrochemical workstation with a three-electrode system, consisting of a Pt wire counter electrode, a saturated calomel electrode (SCE) as reference electrode and a working electrode of PI/CNT-RGO film with an area of 0.1256 cm^2. The film was immersed into a solution of 2×10^{-3} M $(NH_4)_2MoS_4$ containing 0.2 M KCl and 0.2 M NH_4Cl and cyclic voltammograms (CVs) were performed between 0.1 and −1.0 V at 10 mV s^{-1}.[26] All chemicals were of analytical grade and used without further purification. Milli-Q water was used throughout this work.

Characterizations: The morphologies were investigated by a field emission scanning electron microscopy (FE-SEM) (Hitachi S-4800, Japan). The crystalline structures of samples were determined by X-ray diffraction (XRD) (RigakuD/max-2400). Transmission electron microscopy (TEM), high-resolution transmission electron microscopy (HRTEM) images, and selected area electron diffraction (SAED) were performed on a FEI Tecnai G^2 F30 TEM. X-Ray photoelectron spectroscopy (XPS) was obtained on an AXIS ULTRA DLD XPS spectrometer. Raman spectroscopy was performed using a Horiba Jobin Yvon LabRAM Aramis system with a 532 nm excitation laser. Electrochemical measurements were carried out on CHI 660 electrochemical workstation using the same three-electrode setup for electrodeposition. The HER electrocatalytic activity of MoS_2 was investigated by polarization curves using linear sweep voltammetry (LSV) at a scan rate of 10 mV s^{-1} in 0.5 M H_2SO_4 electrolyte at room temperature. The loading weight of MoS_2 was measured by the mass difference between the PI/CNT-RGO and PI/

Table 2. HER parameters of various MoS_2 samples.

Films [CVs]	Tafel slope [mV dec^{-1}]	Exchange current density j_0 [μA cm^{-2}]
5	95	7.76
10	79	9.12
15	61	11.48
20	72	9.77
25	88	8.51
30	103	6.75
PI/CNT-MoS_2	109	5.01

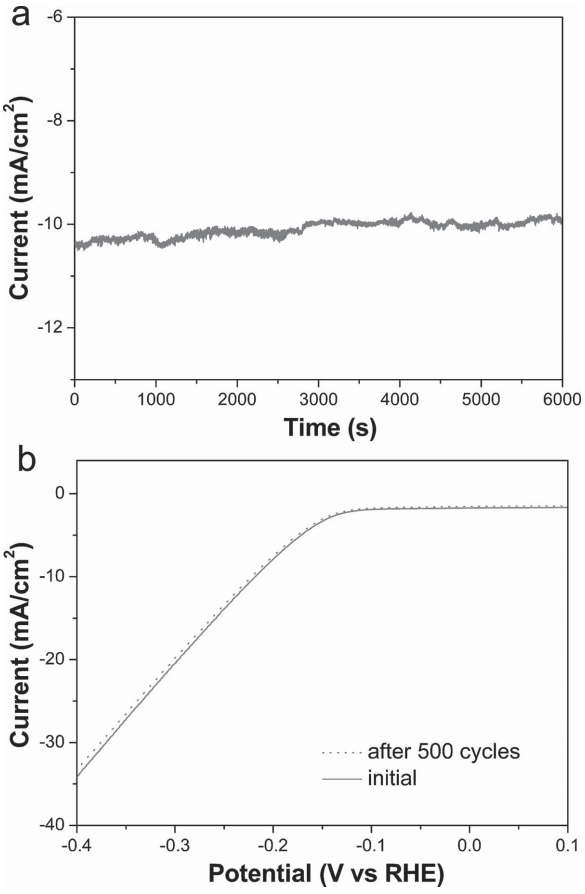

Figure 8. a) Current–time curves under a constant overpotential of 250 mV; b) long-term cycling test for the PI/CNT-RGO-MoS_2 film.

CNT-RGO-MoS_2 films and film area. When the film area was 0.28 cm^2, the mass difference of the two films was less than 0.01 mg, indicating that the loading weight of MoS_2 was less than 0.04 mg cm^{-2}. The cycling test of MoS_2 was performed between 0.1 and –0.4 V at a scan rate of 10 mV s^{-1} in 0.5 M H_2SO_4 (pH = 0.3).

Supporting Information

Supporting Information is available from the Wiley Online Library or from the author.

Acknowledgements

This work was supported by the National Natural Science Foundation of China (Grant No. 51372106).

Received: January 16, 2015
Revised: February 25, 2015
Published online: March 25, 2015

[1] M. S. Dresselhaus, I. L. Thomas, *Nature* **2001**, *414*, 332.
[2] A. J. Bard, M. A. Fox, *Acc. Chem. Res.* **1995**, *28*, 141.
[3] M. G. Walter, E. L. Warren, J. R. McKone, S. W. Boettcher, Q. Mi, E. A. Santori, N. S. Lewis, *Chem. Rev.* **2010**, *110*, 6446.
[4] J. K. Norskov, C. H. Christensen, *Science* **2006**, *312*, 1322.
[5] J. Greeley, T. F. Jaramillo, J. Bonde, I. Chorkendorff, J. K. Nørskov, *Nat. Mater.* **2006**, *5*, 909.
[6] Y. Hou, A. B. Laursen, J. Zhang, G. Zhang, Y. Zhu, X. Wang, S. Dahl, I. Chorkendorff, *Angew. Chem. Int. Ed.* **2013**, *52*, 3621.
[7] Y. Li, P. Hasin, Y. Wu, *Adv. Mater.* **2010**, *22*, 1926.
[8] D. S. Kong, H. T. Wang, J. J. Cha, M. Pasta, K. J. Koski, J. Yao, Y. Cui, *Nano Lett.* **2013**, *13*, 1341.
[9] D. Voiry, H. Yamaguchi, J. Li, R. Silva, D. C. B. Alves, T. Fujita, M. Chen, T. Asefa, V. B. Shenoy, G. Eda, M. Chhowalla, *Nat. Mater.* **2013**, *12*, 850.
[10] H. Vrubel, D. Merkia, X. Hu, *Energy Environ. Sci.* **2012**, *5*, 6136.
[11] Y. Yan, L. Zhang, X. Qi, H. Song, J. Wang, H. Zhang, X. Wang, *Small* **2012**, *8*, 3350.
[12] H. Vrubel, X. Hu, *Angew. Chem., Int. Ed.* **2012**, *51*, 12703.
[13] E. S. Andreiadis, P.-A. Jacques, P. D. Tran, A. Leyris, M. Chavarot-Kerlidou, B. Jousselme, M. Matheron, J. Pécaut, S. Palacin, M. Fontecave, V. Artero, *Nat. Chem.* **2013**, *5*, 48.
[14] X. Hu, B. S. Brunschwig, J. C. Peters, *J. Am. Chem. Soc.* **2007**, *129*, 8988.
[15] J. Xie, H. Zhang, S. Li, R. Wang, X. Sun, M. Zhou, J. Zhou, X. W. Lou, Y. Xie, *Adv. Mater.* **2013**, *25*, 5807.
[16] B. Hinnemann, P. G. Moses, J. Bonde, K. P. Jorgensen, J. H. Nielsen, S. Horch, I. Chorkendorff, J. K. Nørskov, *J. Am. Chem. Soc.* **2005**, *127*, 5308.
[17] T. F. Jaramillo, K. P. Jorgensen, J. Bonde, J. H. Nielsen, S. Horch, I. Chorkendorff, *Science* **2007**, *317*, 100.
[18] L. Liao, J. Zhu, X. Bian, L. Zhu, M. D. Scanlon, H. H. Girault, B. Liu, *Adv. Funct. Mater.* **2013**, *23*, 5326.
[19] Y. Liang, Y. Li, H. Wang, H. Dai, *J. Am. Chem. Soc.* **2013**, *135*, 2013.
[20] Q. H. Wang, K. Kalantar-Zadeh, A. Kis, J. N. Coleman, M. S. Strano, *Nat. Nanotechnol.* **2012**, *7*, 699.
[21] Y. Li, H. Wang, L. Xie, Y. Liang, G. Hong, H. Dai, *J. Am. Chem. Soc.* **2011**, *133*, 7296.
[22] A. B. Laursen, P. C. K. Vesborg, I. Chorkendorff, *Chem. Commun.* **2013**, *49*, 4965.
[23] S. Peng, L. Li, X. Han, W. Sun, M. Srinivasan, S. G. Mhaisalkar, F. Cheng, Q. Yan, J. Chen, S. Ramakrishna, *Angew. Chem. Int. Ed.* **2014**, *53*, 12594.
[24] H. Z. Geng, R. Rosen, B. Zheng, H. Shimoda, L. Fleming, J. Liu, O. Zhou, *Adv. Mater.* **2002**, *14*, 1387.
[25] S. Subramoney, *Adv. Mater.* **1998**, *10*, 1157.
[26] Y. Jiang, S. Yu, J. Li, L. Jia, C. Wang, *Carbon* **2013**, *63*, 367.
[27] Y. Jiang, L. Jia, S. Yu, C. Wang, *J. Mater. Chem. A* **2014**, *2*, 6656.
[28] Y. Liang, Y. Li, H. Wang, J. Zhou, J. Wang, T. Regier, H. Dai, *Nat. Mater.* **2011**, *10*, 780.
[29] D. Merki, S. Fierro, H. Vrubel, X. Hu, *Chem. Sci.* **2011**, *2*, 1262.
[30] K. Chang, W. Chen, *Chem. Commun.* **2011**, *47*, 4252.
[31] S. Wu, C. Huang, G. Aivazian, J. S. Ross, D. H. Cobden, X. Xu, *ACS Nano* **2013**, *7*, 2768.
[32] J.-Y. Lin, C.-Y. Chan, S.-W. Chou, *Chem. Commun.* **2013**, *49*, 1440.
[33] H. J. Shin, K. K. Kim, A. Benayad, S. M. Yoon, H. K. Park, I. S. Jung, M. H. Jin, H. K. Jeong, J. M. Kim, J. Y. Choi, Y. H. Lee, *Adv. Funct. Mater.* **2009**, *19*, 1987.
[34] Y.-H. Lee, X. Q. Zhang, W. J. Zhang, M.-T. Chang, C.-T. Lin, K.-D. Chang, Y.-C. Yu, J. T.-W. Wang, C.-S. Chang, L.-J. Li, T.-W. Lin, *Adv. Mater.* **2012**, *24*, 2320.
[35] Q. He, S. Wu, Z. Yin, H. Zhang, *Chem. Sci.* **2012**, *3*, 1764.
[36] X. Wang, H. Feng, Y. Wu, L. Jiao, *J. Am. Chem. Soc.* **2013**, *135*, 5304.
[37] H. Wang, L.-F. Cui, Y. Yang, H. S. Casalongue, J. T. Robinson, Y. Liang, Y. Cui, H. Dai, *J. Am. Chem. Soc.* **2010**, *132*, 13978.
[38] X.-C. Dong, H. Xu, X.-W. Wang, Y.-X. Huang, M. B. Chan-Park, H. Zhang, L.-H. Wang, W. Huang, P. Chen, *ACS Nano* **2012**, *6*, 3206.
[39] K. Roy, M. Padmanabhan, S. Goswami, T. P. Sai, G. Ramalingam, S. Raghavan, A. Ghosh, *Nat. Nanotechnol.* **2013**, *8*, 826.
[40] J. Kibsgaard, Z. Chen, B. N. Reinecke, T. F. Jaramillo, *Nat. Mater.* **2012**, *11*, 963.
[41] Y. Yan, B. Y. Xia, X. Ge, Z. Liu, J.-Y. Wang, X. Wang, *ACS Appl. Mater. Interfaces* **2013**, *5*, 12794.
[42] C.-B. Ma, X. Qi, B. Chen, S. Bao, Z. Yin, X.-J. Wu, Z. Luo, J. Wei, H.-L. Zhang, H. Zhang, *Nanoscale* **2014**, *6*, 5624.
[43] C. Xu, S. Peng, C. Tan, H. Ang, H. Tan, H. Zhang, Q. Yan, *J. Mater. Chem. A* **2014**, *2*, 5597.
[44] W. Zhou, K. Zhou, D. Hou, X. Liu, G. Li, Y. Sang, H. Liu, L. Li, S. Chen, *ACS Appl. Mater. Interfaces* **2014**, *6*, 21534.
[45] J. D. Benck, Z. Chen, L. Y. Kuritzky, A. J. Forman, T. F. Jaramillo, *ACS Catal.* **2012**, *2*, 1916.
[46] X. Chen, D. Wang, Z. Wang, P. Zhou, Z. Wu, F. Jiang, *Chem. Commun.* **2014**, *50*, 11683.
[47] C. Ge, P. Jiang, W. Cui, Z. Pu, Z. Xing, A. M. Asiri, A. Y. Obaid, X. Sun, J. Tian, *Electrochim. Acta* **2014**, *134*, 182.
[48] B. E. Conway, B. V. Tilak, *Electrochim. Acta* **2002**, *47*, 3571.
[49] N. Pentland, J. O. M. Bockris, E. Sheldon, *J. Electrochem. Soc.* **1957**, *104*, 182.